Title

Bifunctional M13 Bacteriophage Nanospheroids for the Synthesis of Hybrid Noncentrosymmetric Nanoparticles

Journal

ACS Applied Nano Materials, 3(11)

ISSN

2574-0970

Authors

Plank, Joshua M

Alibay, Zaira

Ngo-Duc, Tam-Triet

et al.

Publication Date

2020-11-25

DOI

10.1021/acsanm.0c01876

Peer reviewed

Citation: *ACS Applied Nano Materials 2020 3 (11), 10668-10677*

Bifunctional M13 Bacteriophage Nanospheroids for the Synthesis of Hybrid Non-Centrosymmetric Nanoparticles

Joshua M. Plank,[1] *Zaira Alibay,*[2] *Tam-Triet Ngo-Duc,*[2] *Michelle Lai,*[3] *Eleanor A. S. Mayes,*[2,‡] *Elaine D. Haberer*[1,2,*]

[1]Department of Electrical and Computer Engineering, University of California, Riverside 92521, USA

[2]Materials Science and Engineering Program, University of California, Riverside 92521, USA

[3]Department of Chemical and Environmental Engineering, University of California, Riverside 92521, USA

[‡]Present Address: Department of Chemical Engineering and Materials Science, University of Minnesota 55455, USA.

Keywords: Material template, M13, spheroid, asymmetric nanostructures, bacteriophage, heterostructure

ABSTRACT: Non-centrosymmetric nanostructures are composed of two different materials displayed on spatially distinct surface regions. These nontrivial building blocks facilitate self-assembly of hierarchical nanostructures with increased complexity and support cooperative material behaviors. The arrangement of M13 bacteriophage structural proteins within its capsid creates a promising monodisperse and readily modifiable template for these low symmetry nanomaterials. Here, a 9-mer ZnS-binding peptide was inserted into the p3 minor coat protein (capsid tip) of an M13 bacteriophage with Au-binding motif fused to its p8 major coat protein (capsid body). Multiple vortex/rest cycles with chloroform were used to convert this bifunctional, Au/ZnS (p8/p3)-binding phage from filament to spheroid. The shape transformation was studied with transmission electron microscopy, circular dichroism spectroscopy, and fluorescence spectroscopy. The effects of the p3 peptide fusion and conversion temperature were evaluated. Compared to the Au-binding phage without a p3 peptide fusion, the insertion of the ZnS-binding motif increased spheroid size, molar ellipticity loss, and intrinsic fluorescence quenching. Reduced temperature (0°C) within early transformation cycles diminished spheroid polydispersity and increased agglomeration resistance. In addition, Au/ZnS-binding spheroids retained peptide motif affinity and relative placement of the p3 and p8. Site-specific synthesis of ZnS and Au on the p3 and p8, respectively, produced non-centrosymmetric hybrid metal/semiconductor nanostructures. This work highlights the effect of a p3 mutation on filament to spheroid transformation as well as the importance of temperature in producing a robust scaffold for inorganic material synthesis. Lastly, the manufactured bifunctional M13 spheroids were used for bio-directed synthesis of non-centrosymmetric nanoparticle assemblies demonstrating the potential for heterojunction formation.

1. INTRODUCTION

Viral capsids are monodisperse, self-assembled biomolecular complexes. They display both a large variety and high density of functional moieties on their surface. Their structure and chemistry, including exact shape and site-specific functional groups, are genetically encoded and known with atomic scale precision. Notably, this benchmark is unrivaled by synthetic nanoparticles. These exquisite multivalent nanoscale building blocks have demonstrated both short- and long-range control over materials synthesis and assembly.[1–3] Yet, the high symmetry and functional site equivalence of these proteinaceous scaffolds limit building block directionality and prevent assembly of more complex inorganic structures. Lower symmetry viral nanoparticles with reduced surface homogeneity are required.

Among the more complex inorganic structures of interest are dual-component nanoparticles that consist of two different materials displayed on opposing surface regions. These intrinsically directional particles have recently gained attention in fields ranging from biomedical[4] to solar energy.[5] The architecture has the distinction of spatially separating functionalities, enabling novel or enhanced performance unattainable with uniform surface chemistry. For example, these asymmetric particles can simultaneously deliver hydrophobic and hydrophilic drug therapies,[6,7] speed analyte detection via self-electrophoresis,[8] or manipulate photogenerated charge separation to enhance photocatalytic performance.[9] These remarkable tasks are difficult, or even impossible with single component or concentric core-shell nanoparticles. While a number of manufacturing methods have been explored,[10,11] most of have focused on two-sided particles a few microns or hundreds of nanometers in size. Reports of sub-100 nm particles have been less common. Structural and functional asymmetry can be challenging to achieve at these length scales with synthetic processes.

The spheroidal form (s-form) of the M13 bacteriophage is a viral template that has the potential to both overcome the symmetry constraints associated with most other viruses and answer fabrication challenges related to sub-100 nm non-centrosymmetric particles. In its native filamentous form, the capsid of this combinatorial phage display mainstay is composed of five structural proteins: four minor coat proteins (p3, p6, p5, p9) and one major coat protein (p8). Of these, the p3 and p8 are regularly used for identification of affinity peptides, as well as inorganic material assembly.[12,13] Approximately 2700 copies of the small, α-helical p8 protein form a tube-like structure around the viral DNA to comprise the M13 body,[14] while five copies of the much larger p3 protein cap its distal end. With simple exposure to a chloroform/water interface, this relatively low symmetry, filamentous bacteriophage undergoes a dramatic morphological transformation that mimics the host infection process. Changes in hydrophobic interactions among the p8 coat proteins cause them to slide past one another, and two-thirds of the viral DNA is extruded through a single pore located near the p3 site.[15] Thus, the nearly one micron long filament becomes a spheroid tens of nanometers in diameter with a non-centrosymmetric protein arrangement. Using the native arrangement of the filamentous phage capsid avoids complicated multi-step, low yield processes often used for breaking viral symmetry such as toposelective surface modification[16,17], stoichiometric assembly,[18] and DNA scaffold engineering.[19] Whereas monofunctional M13 spheroids with affinity peptides uniformly displayed on p8 major coat proteins have been used for materials synthesis and assembly,[20,21] bifunctional spheroids suitable as sub-100 nm non-centrosymmetric particle scaffolds have yet to be explored.

This study examines the conversion of Au/ZnS (p8/p3)-binding M13 filaments into nanospheroids, then uses the unique asymmetric structural protein arrangement within the bifunctional viral scaffold to direct synthesis of metal/semiconductor non-centrosymmetric

hybrid nanomaterials. A series of vortex/rest cycles in the presence of chloroform was used to alter the geometry of the phage. Particular attention was given to the effect of the p3 peptide fusion and temperature on transformation. The conversion process was characterized via circular dichroism, fluorescence spectroscopy, and transmission electron microscopy. Surprisingly, the ZnS-binding peptide fusion strongly influenced the transformation process. The motif caused bifunctional Au/ZnS-binding spheroids to be larger in size, display a greater loss of molar ellipticity, and experience more quenching of intrinsic fluorescence than monofunctional Au-binding spheroids without a ZnS-binding peptide. A comparison of Au/ZnS-binding phage transformed using room- and low- temperature processes revealed that low temperature produced monodisperse spheroids that were less susceptible to agglomeration. These robust, bifunctional nanospheroids were used in the site-specific growth of hybrid metal/semiconductor nanostructures, via sequential synthesis of ZnS on p3 and Au on p8. The retained functionality of both minor and major coat fusion peptides for materials synthesis is noteworthy. The unique, asymmetric placement of the p3 and p8 proteins within the bifunctional M13 spheroid presents a rare opportunity for viral-templated production of hybrid, sub-100 nm non-centrosymmetric assemblies. Such nanostructures have potential to critically enhance performance in a range of drug delivery, sensing, and catalysis applications.[22,23]

2. EXPERIMENTAL DETAILS

2.1 Bifunctional M13 bacteriophage clone preparation and chloroform transformation. As a model for the study of bifunctional M13 nanospheroid formation, a Au/ZnS (p8/p3)-binding M13 bacteriophage was prepared. Using previously reported methods, a Au-binding motif, VSGSSPDS,[24] was displayed on the N-terminus of each p8 protein along the length of the virus and a constrained ZnS-binding peptide, CNNPMHQNC,[25] was displayed on the N-terminus of

each p3 protein at its proximal end.[24,26] For comparison, a Au-binding phage without a p3 peptide fusion was also prepared, as well as an unmodified or wild-type phage (M13KE, New England Biolabs). Filamentous M13 phage were converted to spheroids using a chloroform treatment process.[15,20] Phage solutions were suspended in 100 μL of tris-buffered saline (TBS, 50 mM Tris–HCl, 150 mM NaCl, pH 7.5) at a concentration of 10^8 pfu/μL to which an equal volume of amylene-stabilized chloroform (99.8%, ACROS Organics) was added. The mixture was vortexed at room temperature at high power for one vortex/rest (2 s/13 s) cycle followed by up to seven additional vortex/rest cycles at low power. After mixing, approximately 85 μL of chloroform was withdrawn with a pipette. The remaining chloroform was removed by gently flowing air over the sample. Phage solutions were immediately cooled at 4°C and prepared for subsequent characterization. To elucidate the effect of transformation temperature on M13 spheroid formation, some transformations were performed in which the first three vortex/rest cycles were held at 0°C. This approach, adapted from previous reports,[27] was intended to yield rod-shaped intermediates or i-forms which were converted to spheroids in subsequent cycles. Equal volumes (100 μL) of filamentous M13 phage and chloroform were chilled at 0°C for 20 s, combined, then vortexed at 0°C. Following the third vortex/rest cycle, samples were quickly warmed in a 37°C water bath for 20 s. Additional vortex/rest cycles were completed at room temperature. Hereafter, this transformation procedure will be described as low temperature (LT). To assess nanospheroid stability against agglomeration, templates formed using 5 cycles vortex/rest cycles were stored at 4°C in TBS buffer. Stability was evaluated by measuring the areal density of spheroids and agglomerates with transmission electron microscopy (TEM) as a function of storage time. Measurements were taken on three independent samples and averaged.

2.2 ZnS and Au synthesis. Assembly of non-centrosymmetric, dual component nanostructures was demonstrated using Au/ZnS-binding spheroids produced with the LT chloroform treatment procedure and 5 vortex/rest cycles. ZnS and Au were synthesized sequentially on these s-form Au/ZnS-binding phage using adapted procedures.[20,24] The p3 minor coat protein was targeted for ZnS synthesis. A 10 μM solution of zinc chloride ($ZnCl_2$, Sigma Aldrich) was prepared with viral templates at a concentration of 10^8 pfu/μL in TBS. The solution was stored at 4°C for 3 h, and then an equal volume of 10 μM sodium sulfide (Na_2S, Sigma Aldrich) was added dropwise in 10 μL volumes at room temperature over the course of an hour. The entire solution was incubated at room temperature for an additional 6 h. Residual ZnS precursors were removed via centrifugal filtration (Amicon Ultra-0.5, 3 kDa) and synthesis products were resuspended in TBS. The p8 major coat protein was targeted for Au synthesis. A 100 μL volume of 5 x 10^7 pfu/μL phage was mixed with sodium borohydride ($NaBH_4$, Sigma Aldrich) to achieve a 1 μM solution. Subsequently, 2.5 μL of chloroauric acid ($HAuCl_4$, Sigma Aldrich) was added for a final concentration of 150 μM. Reducing agent was added first to mitigate undesirable interactions between $HAuCl_4$ and ZnS. Samples were immediately prepared for TEM and spectroscopic measurements. As controls, Au/ZnS-binding filaments and wild-type viral templates were also used for ZnS and Au synthesis.

2.3 Circular dichroism (CD) and fluorescence measurements. Changes in the secondary structure of the p8 protein were monitored after each vortex/rest cycle from 0 to 8 using a circular dichroism (CD) spectrometer (Jasco J-815). Room temperature CD scans were taken from 200-250 nm with the following parameters: 50 nm/min scan speed, 1 nm band width, 4 s response time, and 12 scan accumulation. The mean and standard deviation for measurements taken on three independent samples were reported.

Cycle-by-cycle analysis of changes in the local tryptophan environment was completed with a spectrofluorometer (Quanta Master 400). Room temperature fluorescence scans were taken from 270-400 nm with the following parameters: 5 nm slit widths, 1 s integration time, 1 nm step size, and 255 nm excitation source. The mean and standard deviation for measurements taken on three independent samples were reported.

2.4 Transmission electron microscopy (TEM) characterization, zeta potential measurements, and dynamic light scattering (DLS) measurements. Transmission electron microscopy (TEM, Tecnai T12 or S/TEM Titan Themis 300) was used to study viral template geometry and size, as well as the morphology, size, site-specific growth, and overall viral template coverage of ZnS and Au synthesis products. Electron diffraction (ED) and high resolution TEM (HRTEM) were used to determine the crystal structure of the synthesized materials. Elemental analysis of the synthesis products was completed using energy dispersive spectroscopy (EDS).

To prepare TEM samples for imaging and diffraction, a 5 μL volume of solution was added to a formvar/carbon-coated copper grid (Ted Pella, Inc), incubated 5 minutes, and washed twice with deionized water. Viral template samples without ZnS or Au were stained with 2% uranyl acetate for 30 s, then wicked dry. To prepare synthesis products and remove precursors, ED and EDS samples were pelleted three times at 14,000 rpm for 15 min and resuspended in deionized water, then 20 μL of concentrated product was dropcasted onto a SiN grid (Electron Microscopy Sciences).

Image processing and analysis were completed with ImageJ software. A minimum magnification of 11,000x was used to determine template size and differentiate among templates

(spheroids, i-forms, and filaments). An ellipse was fit to each template to compute spheroid size, and major and minor axes were measured and averaged. The long and short axes of i-forms and filaments were measured directly. Template aspect ratio was used to distinguish spheroids (< 3), intermediate forms (3 - 25), and filaments (> 25). Low aspect ratio particles (< 3) larger than 150 nm were classified as agglomerates. Areal densities of viral templates were evaluated in 10 randomly selected grid locations for three different samples and averaged. The size of ZnS and Au synthesis products was determined by averaging long and short particle axes.

The particle size and zeta potential of the M13 spheroids was measured using dynamic and electrophoretic light scattering (Zetasizer, ZS90), respectively. For each analysis technique, three 25 scan measurements were taken of three samples and averaged.

3. RESULTS AND DISCUSSION

3.1 Room temperature transformation of bifunctional M13 bacteriophage. An overview of the simple, chloroform-based process used to transform bifunctional M13 filaments into nanospheroidal templates for non-centrosymmetric, inorganic nanostructures is shown in Figure 1. The Au/ZnS-binding phage were filaments approximately 960 nm long before chloroform treatment, as the viral capsid length is determined by the enclosed genome. The geometric change of the Au/ZnS (p8/p3)-binding phage was initially examined at room temperature using electron microscopy, CD, and intrinsic fluorescence. To evaluate the effect of the ZnS-binding p3 peptide insert on bifunctional template conversion and functionally asymmetric nanospheroid formation, these data were compared to those of a monofunctional Au-binding phage without a minor coat protein fusion prepared under the same conditions.

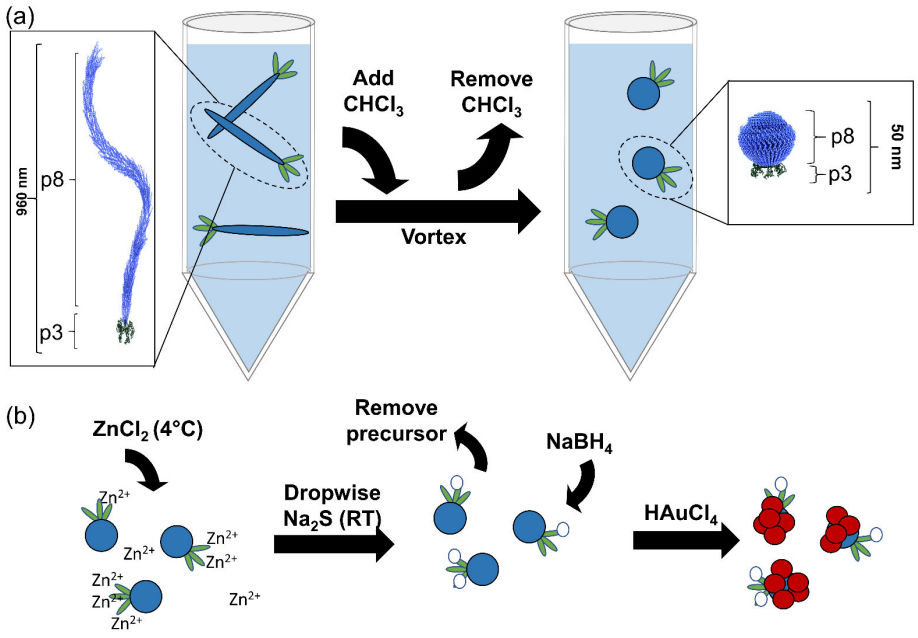

Figure 1. Scheme for synthesis of hybrid non-centrosymmetric nanoparticles using bifunctional bacteriophage nanospheroids. (a) Shape transformation of M13 bacteriophage. To convert the filamentous viruses to spheroids, solutions were mixed with chloroform and briefly, but repeatedly vortexed, pausing between cycles. During this process, the nearly micron long filamentous capsid gradually contracted into a spheroid tens of nanometers in size. The positional asymmetry of the p3 minor and p8 major coat proteins found within the filamentous form was preserved within the spheroidal form. As a result, these proteins were employed in directed synthesis of non-centrosymmetric nanomaterials. (b) To synthesize Au/ZnS nanostructures, $ZnCl_2$ was incubated at 4°C with bifunctional Au/ZnS-binding spheroids to bind Zn ions, and then Na_2S was added dropwise at room temperature (RT). After an additional incubation step, ZnS nanoparticles were formed on the p3, and remaining precursors were removed via centrifuge filtration. Subsequently, to form Au nanoparticles on the p8, $NaBH_4$ was added, followed by $HAuCl_4$.

Knowledge of and, ultimately, control over nanospheroid morphology and size are essential for design of non-centrosymmetric, inorganic structures. For this reason, the conversion of the Au/ZnS-binding phage was analyzed after each vortex/rest cycle. Representative TEM images depicting changes in template morphology and corresponding viral template areal densities are shown in Figure S1 and Figure S2, respectively. Initially, the transformation proceeded inhomogeneously, producing a mixture of filaments, intermediate forms (i-forms), and spheroids (s-forms). With each vortex/rest cycle, the number of filaments and i-forms decreased as the number of spheroids increased. In addition to the observed shape modification, it was noted that s-form size increased on average from 54 to 68 nm within the first 3 vortex/rest cycles, and

continued to slowly expand to 85 nm by cycle 8 (Figure S3). A similar gradual progression in transformation and spheroid enlargement was observed in Au-binding phage without a p3 peptide, albeit with a slightly different relationship to vortex/rest cycle.[20] Because no filaments were found after 5 vortex/rest cycles and a relatively high yield of nanospheroids was achieved, these templates were selected for further study. As illustrated in Figure 2a and further supported by Figure S4, these Au/ZnS-binding spheroids displayed the rounded, slightly deflated morphology that is characteristic of filamentous Ff class spheroids.[15,20,27,28] The size distribution and average size (77 ± 21 nm) of these spheroids, as determined by TEM, is shown in Figure 2b. The hydrodynamic radius and zeta potential of the spheroids, as measured by light scattering analysis, were 134 ± 56 nm and 17.7 ± 1.5 mV (Figure S4), respectively. Interestingly, Au/ZnS-binding spheroid size was appreciably larger than that reported for Au-binding spheroids at the same cycle number (Figure S3), indicating a clear effect of the added p3 insertion on spheroid formation and size.[20]

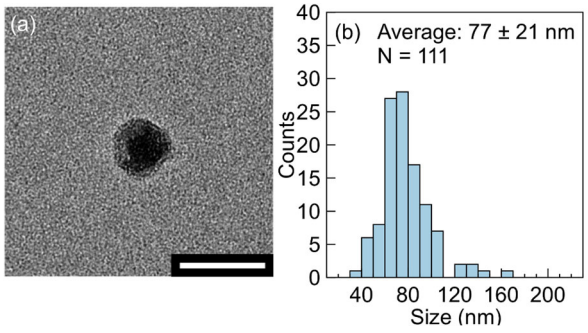

Figure 2. Au/ZnS-binding spheroid (a) morphology and (b) size distribution following 5 vortex/rest cycles with chloroform at room temperature. Samples were stained with 2% uranyl acetate. Scale bar: 100 nm.

CD spectroscopy was used to correlate template morphology observed with TEM to changes in viral protein conformation. Spectra of the Au/ZnS-binding phage are shown in Figure 3a as a function of vortex/rest cycle, along with the amino acid sequence of the Au-binding M13 p8 coat protein and its helical secondary structure within the filament in Figure 3b.[29–31] Because 85% of the M13 viral capsid mass is attributed to the p8 major coat protein, its structure dominated the CD spectrum and allowed conformational changes to be monitored throughout the transformation process.[32,33] The spectrum of the filamentous phage was dominated by a negative peak in molar ellipticity at 222 nm which decreased in magnitude with each successive vortex/rest cycle. This peak represents the combined absorption of the p8 α-helix and the chromophore coupling of W26 and F42/F45 residues on neighboring p8 proteins. In Figure 3c, the molar ellipticity of the Au/ZnS-binding phage at 222 nm is plotted. The Au/ZnS-binding phage underwent a dramatic decrease in the 222 nm peak magnitude during the first two vortex/rest cycles, followed by a modest decrease in subsequent cycles. The reduction in ellipticity has been attributed to a combination of helicity loss and altered hydrophobic interactions among p8 coat protein sidechains that causes them to slide past one another. The most significant decrease was concurrent with the vortex/rest cycles in which TEM showed that the majority of filaments had contracted to form spheroids (Figure S2); the subsequent, more minor decline was associated with the transformation of the remaining filaments and the gradual expansion of existing s-forms (Figure S3). For comparison, cycle-by-cycle molar ellipticity values are also shown from the literature for the Au-binding phage.[20] Overall, the Au/ZnS-binding phage spheroids retained 20% less molar ellipticity at 222 nm, and experienced a larger change in secondary structure than the Au-binding phage spheroids. The difference in ellipticity between the bifunctional Au/ZnS-binding and monofunctional Au-binding phage was associated

with higher spheroid conversion in initial cycles and larger spheroid size in later cycles. Both are important considerations for viral scaffold formation.

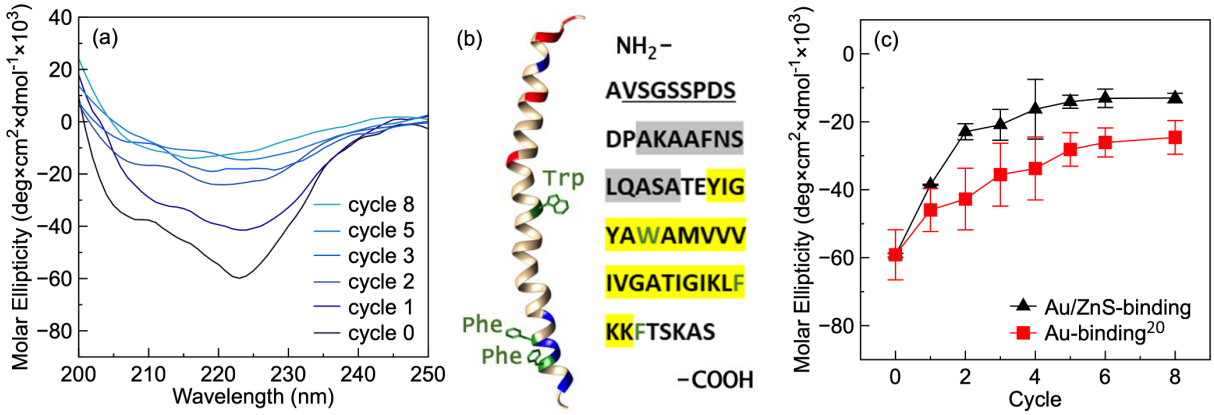

Figure 3. (a) Circular dichroism (CD) spectra of Au/ZnS-binding phage exposed to an increasing number of vortex/rest cycles at room temperature. Spectra were smoothed using a 5 point Savitsky-Golay filter. (b) The secondary structure of the p8 coat protein and corresponding amino acid sequence. The Au-binding peptide sequence is underlined. Grey and yellow highlighted text show amphipathic and hydrophobic helical regions, respectively.[30] Within the molecular model, negative, positive, and aromatic residues are indicated in red, blue, and green, respectively. Molecular visualization was performed using Protein Data Bank record 2C0W and UCSF Chimera.[29 30 31] (c) Molar ellipticity as a function of cycle number at 222 nm for both the Au/ZnS-binding and Au-binding phage.[20] Mean and standard deviation are reported for measurements from three independent samples.

Using fluorescence spectroscopy, the same cycle-by-cycle approach was applied to further investigate changes within the viral capsid during transformation. Intrinsic fluorescence is a strong indicator of the local protein environment, and is often used to complement secondary structure information obtained by CD spectroscopy. Modifications in the tryptophan environment manifest as wavelength shifts and/or emission quenching. Figure 4a presents the emission spectra of the Au/ZnS-binding phage. Fluorescence was primarily dictated by the tryptophan residue, W26, located within hydrophobic region of the p8 protein and in close proximity to the F42/F45 residues on neighboring p8 proteins.[33] As shown in Figures 4b and 4c, over 8 vortex/rest cycles, the peak wavelength decreased only 10 nm, while the relative peak

intensity was reduced by nearly 80%. The relatively small blue shift paired with significant emission quenching in Au/ZnS-binding phage indicated a minimal difference in the polarity of the tryptophan environment, but considerable loss of aromatic residue coupling (W26 and F42/F45) within the viral capsid.[28,30,34] Although a comparable wavelength shift was recorded for both Au/ZnS- and Au-binding phage, the Au/ZnS-binding phage exhibited appreciably more quenching (~30%) between cycles 4 and 8. The larger reduction in fluorescence intensity between cycles 4 and 8 signals rapid displacement of the p8 major coat proteins with respect to one another as sidechain packing transitions from rigid to nonrigid.[34] These overall observations were consistent with the aforementioned greater loss of helicity and the notably larger size of the Au/ZnS-binding spheroids, as compared to that reported for Au-binding spheroids.[20]

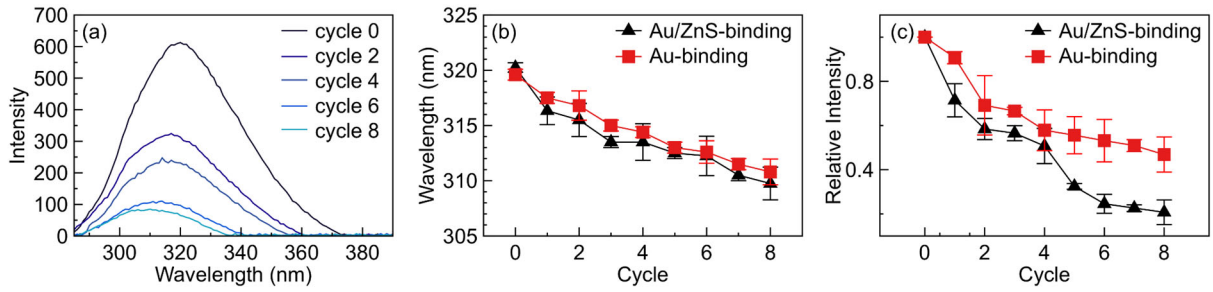

Figure 4. (a) Representative fluorescence spectra of Au/ZnS-binding M13 bacteriophage chloroform treated at room temperature, as well as (b) peak wavelength and (c) relative peak intensity for each vortex/rest cycle. Mean and standard deviation are reported for measurements from three independent samples. For comparison, the peak wavelength and relative intensity of Au-binding phage without a p3 peptide insert are also shown.

Our analysis of the Au/ZnS- and Au-binding spheroid conversion process using electron microscopy, CD, and intrinsic fluorescence indicated that the addition of the ZnS-binding peptide fusion to the p3 minor coat protein caused the filament to spheroid conversion and subsequent expansion of spheroid size to progress further in fewer cycles. These findings are significant as they indicate that, with additional design, the p3 peptide fusion may serve as a

handle with which to control not only the affinity, but also the transformation and size of the bifunctional viral scaffold. While the exact mechanism for observed differences in chloroform transformation with the introduction of a p3 peptide fusion remains unclear, we propose two potential explanations for our findings. First, mutations near the N-terminus may cause partial unfolding of the p3 protein,[35] exposing its otherwise buried hydrophobic region and promoting chloroform interaction.[36] Because the p3 and p6 work cooperatively to cap the proximal end of the M13 virus and maintain the integrity of the assembled major coat protein, increased interaction of the p3 with chloroform may hasten transformation.[36–38] Alternatively, the p3 may dictate the arrangement of the major coat proteins within the viral capsid, and a mutation to the p3 could modify neighboring p8 protein interactions, allowing increased chloroform access and altering the conversion process.[39] Interestingly, other researchers have reported that transformation was not affected by the p3, but purely dependent on the arrangement of the major coat protein.[15,27,40] In those studies, filamentous phage were subjected to subtilisin digestion or French pressure cell shearing to remove part or all of the p3 protein. Yet, subsequent analysis focused primarily on the presence of converted structures without more rigorous characterization of secondary structure, morphology, size, or agglomeration, therefore subtle differences in transformation, such as those observed here, could have been overlooked.

3.4 Low temperature (LT) transformation of bifunctional M13 bacteriophage.

A transformation process adapted from previous reports,[27,34] in which wild-type spheroids were formed from i-forms rather than directly from filaments, was also studied in an effort to better understand the effect of the stepwise shape transition on bifunctional template properties and performance. Here, the conversion scheme was similar to that shown in Figure 1; however, the first 3 cycles of the transformation process occurred at 0°C, followed by additional room

temperature cycles. Au/ZnS-binding M13 capsid morphologies after 3 and 5 vortex/rest cycles are shown in Figures 5a and 5b, while associated viral template areal densities are plotted in Figure S5. Similar to the room temperature procedure, initial vortex/rest cycles produced a blend of filaments, i-forms, and spheroids. Because of the reduced temperature, rather than spheroids, i-forms were the prevailing template structure in early cycles. These i-forms, approximately 140 nm in length, contracted during subsequent room temperature cycles until only s-forms remained (Figure S5). For comparison to room temperature transformation, the spheroid size distribution and average size (45 ± 13 nm) were evaluated with TEM after 5 vortex/rest cycles, and are found in Figure 5c. In addition, several examples of LT spheroid morphology found after 5 cycles are shown in Figure S6. Notably, spheroids produced from i-forms using the LT procedure were about 32 nm smaller and more uniform in geometry and size than those created directly from filaments. A similar trend was observed with light scattering measurements in which a hydrodynamic diameter of 88 ± 25 nm and zeta potential of 21.2 ± 1.2 mV were found (Figure S6). Unlike spheroids produced at room temperature, a minimal increase in size was observed up to cycle 6 (Figure S7). The smaller size and lack of expansion are consistent with cycle-by-cycle CD data (Figure 5d) which revealed a lower overall loss in 222 nm molar ellipticity compared to the room temperature transformation process. Similarly, as shown in Figure 5, the blue shift and emission quenching associated with the LT process were smaller in magnitude and more gradual than for spheroids created with the room temperature process, indicating less displacement of major coat proteins. The cooled cycles appear to have trapped the capsid in the transition between filament and spheroid structures.[27] As evidence, in Figure S8, if all vortex/rest cycles were held at 0°C, i-form contraction halted and i-form length remained constant. These results are in agreement with previous studies, which showed that if the

chloroform/water interaction occurs at low temperatures, the telescoping effect can be halted, producing asymmetric rod-like i-forms with a slight flare near the p3 end.[27,40,41] The temperature-induced pause in transformation reduced the assortment of template geometries and avoided further deterioration of p8-p8 interactions in subsequent vortex/rest cycles, ultimately focusing template geometry and increasing spheroid monodispersity. Uniform template dimensions are essential for the synthesis of asymmetric nanostructures with a narrow size distribution.

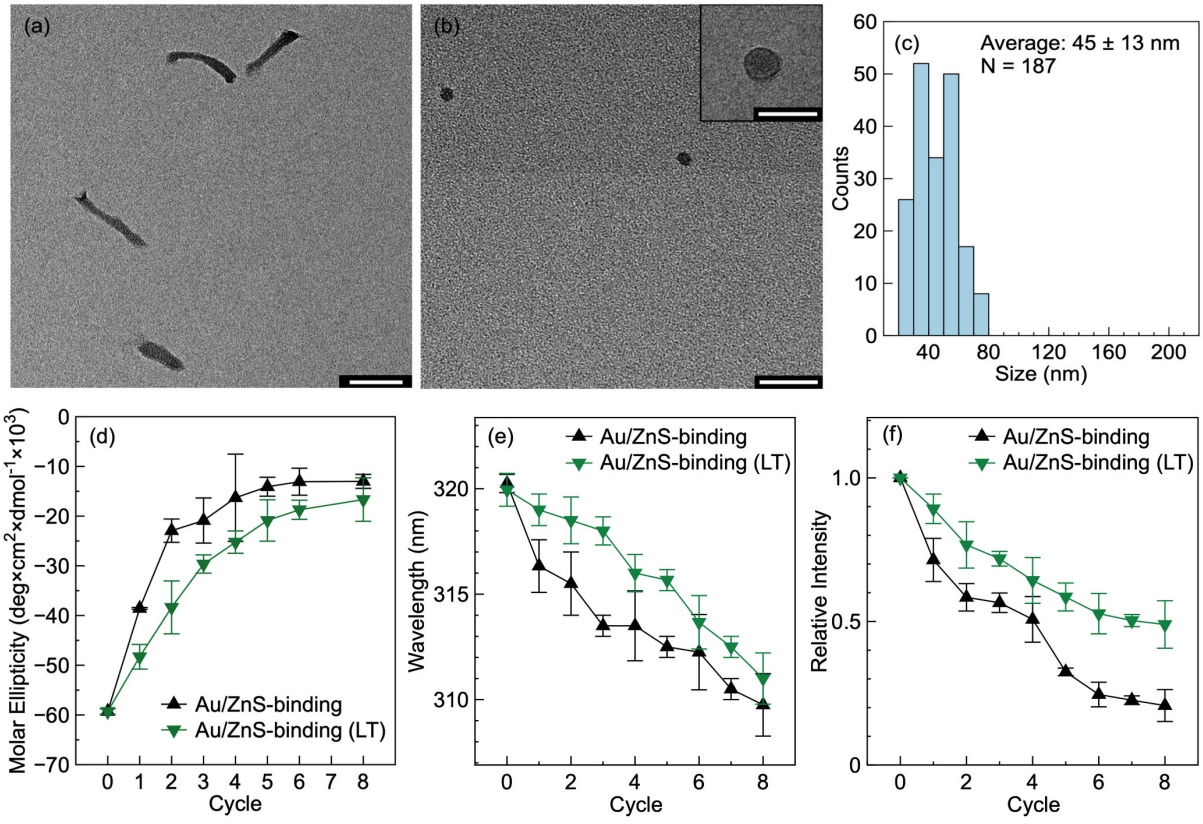

Figure 5. TEM images of Au/ZnS-binding phage after (a) 3 cycles and (b) 5 cycles; scale bar: 100 nm. Inset: High magnification TEM image of individual M13 template; scale bar: 50 nm. Samples were stained with 2% uranyl acetate. (c) A histogram of nanospheroid sizes produced using 5 cycles of the LT transformation process. (d) Molar ellipticity as a function of cycle number at 222 nm for room temperature and low temperature (LT) transformation methods. The first three vortex/rest cycles were held at 0°C for LT transformation. Fluorescence (e) peak shift and (f) quenching observed in Au/ZnS-binding phage for room temperature and LT transformation methods. Mean and standard deviation are reported for measurements from three independent samples.

Spheroid stability, which is critical for templated synthesis of non-centrosymmetric nanostructures, was investigated as a function of transformation temperature. As shown in Figure 6, when stored in TBS buffer at 4°C, the areal density of spheroid templates generated using the room temperature procedure decreased rapidly with time as the agglomerate density increased. Within 10 hours of spheroid formation, only 16% of the initial spheroid density remained, whereas the agglomerate density nearly quadrupled. In contrast, spheroids created using the LT process were much less susceptible to agglomeration, retaining as much as 80% of initial areal density over the same period. The compact structure of these smaller, more monodisperse spheroids may limit solvent exposure of hydrophobic residues within the p3 or p8 proteins (particularly those that terminate the phage body), reducing agglomeration. Au/ZnS-binding spheroids produced via the LT approach with 5 vortex/rest cycles were more robust than those generated at room temperature, and were therefore used for M13 spheroid-directed synthesis of asymmetric hybrid nanomaterials.

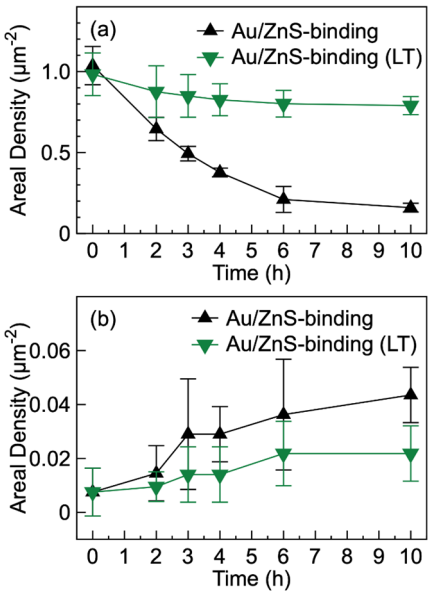

Figure 6. Areal density of Au/ZnS-binding (a) spheroids and (b) agglomerates observed with TEM as a function of storage time. Spheroids produced with both room temperature and LT conversion processes were explored. Viral templates were stored in TBS buffer at 4°C following transformation. A minimum of 100 particles were evaluated on each of three samples to determine the mean and standard deviation of areal density.

3.5 Application of a bifunctional nanospheroid template for synthesis of non-centrosymmetric Au and ZnS nanostructures.

The Au/ZnS-binding M13 nanospheroid was used as a non-centrosymmetric bifunctional template for asymmetric nanostructure assembly. The p3 minor coat protein was targeted for ZnS synthesis and the p8 major coat protein was targeted for Au synthesis. The nanospheroids and related synthesis products were examined after each synthesis step. Following the 10 h ZnS synthesis, the highly stable LT spheroids remained largely intact expanding only a few nanometers in size to 48 ± 14 nm (Figure S9), while template agglomeration increased by a factor of 3. The larger number of agglomerates was attributed to non-specific, electrostatic screening of the spheroid surface charge by Zn ions.

Similar behavior has been observed for M13 filaments.[42] Despite the dramatic change in viral shape, as shown in Figure 7, nanoparticles 5.1 ± 1.4 nm in size with an average aspect ratio of 1.23 were found on approximately 72% of the non-agglomerated Au/ZnS-binding spheroids. A single particle was observed on most spheroids; however, a few templates displayed up to 2 or 3 particles (Figure S10). The small number of localized particles synthesized per spheroid was consistent with selective p3 growth, signaling that chloroform-treatment and viral reconfiguration did not affect the utility of this minor coat protein as an inorganic material scaffold.

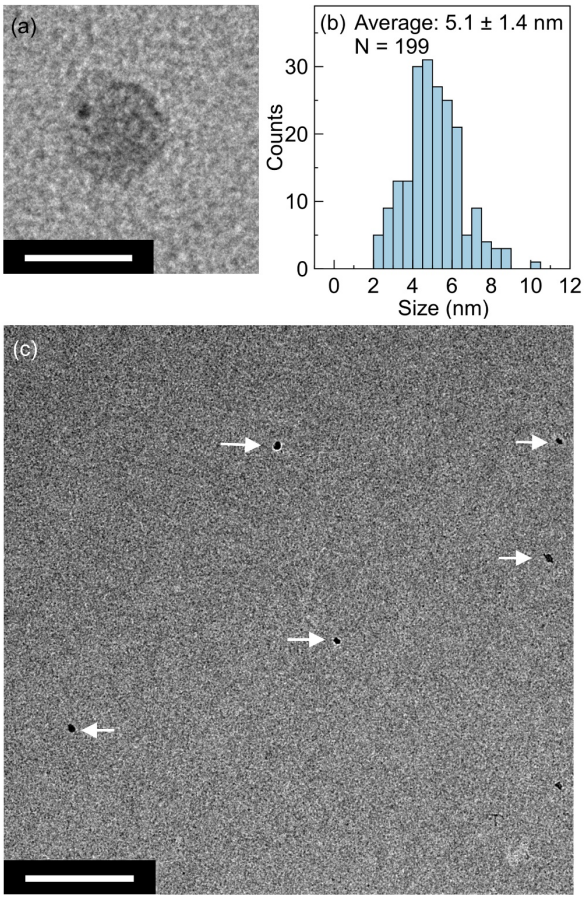

Figure 7. (a) Representative TEM image of ZnS nanoparticle synthesized on a Au/ZnS-binding spheroid; scale bar: 50 nm. (b) Histogram of spheroid-templated ZnS nanoparticle size distribution. (c) Low magnification TEM image of spheroids following ZnS synthesis. Spheroids are indicated by white arrows; scale bar: 500 nm. Samples were not stained prior to imaging.

The crystalline structure of templated synthesis products was determined using electron diffraction. As described in Figure 8 and Table S1, observed lattice fringes and measured d-spacings were indexed to interplanar spacings of both hexagonal and cubic ZnS structures, indicating that a mixture of the two polytypes was synthesized. As earlier reports of ZnS synthesis directed by the same peptide (CNNPMHQNC) produced only wurtzite ZnS on both the filamentous form of the M13 bacteriophage and the icosahedral P22 virus,[26,43] the presence of the cubic form of ZnS was unexpected. Nonetheless, the peptide previously also demonstrated affinity for polycrystalline sphalerite (cubic ZnS)[26] such that synthesis of both polytypes under altered growth conditions was reasonable. For comparison, ZnS was also synthesized under the same conditions using filamentous Au/ZnS-binding, filamentous Au-binding, and wild-type phage (filaments and spheroids), as well as without a phage template. Synthesis product morphology and structure are described in Figures S11 and S12. Crystal structure information is shown in Table S2. The template shape did not largely affect the average ZnS nanoparticle size or the number of ZnS particles per template synthesized on the p3 minor coat protein; however, there was an effect on the overall morphology of the template materials. Unlike Au/ZnS-binding spheroids, filaments formed micelle-like structures around ZnS particles. No ZnS growth was observed on Au-binding phage without a ZnS-binding p3 insert or wild-type filaments or spheroids (Figure S11), and large, highly amorphous ZnS particles were synthesized without a viral template (Figure S12). Both results highlight the critical role the ZnS-binding peptide played in synthesis under the reported conditions.

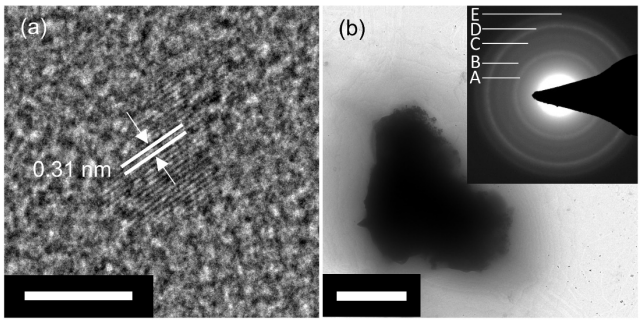

Figure 8. (a) HRTEM image of spheroid-templated ZnS nanoparticle. The denoted lattice fringes corresponded to ZnS zinc-blende (111) and wurtzite (002) interplanar distances; scale bar: 5 nm. (b) TEM image of concentrated spheroid-templated ZnS synthesis products; scale bar: 500 nm. Inset: Selected area electron diffraction pattern of crystalline ZnS material indexed to hexagonal and cubic crystallographic planes in Table S1.

To construct asymmetric hybrid metal/semiconductor nanoparticle assemblies, Au was synthesized on the same spheroidal templates. As revealed in Figure 9, a median of 13 nanoparticles, 7.9 ± 1.5 nm in size, and occasionally fused together were templated on the surface of the spheroids. The relative spatial homogeneity of the nanoparticles on the spheroidal template was consistent with p8-directed synthesis.[20] As shown in Figure 10, lattice fringes from one of many discrete nanoparticles on the spheroid surface revealed an interplanar spacing of 0.23 nm, which is consistent with Au (111). For comparison, Au was also synthesized under the same conditions with Au/ZnS-binding filaments, wild-type phage (filaments and spheroids), and without a template (Figure S13). In all cases, nanoparticles were smaller in size and fewer in number than those templated by Au/ZnS-binding spheroids. These results are consistent with Au synthesis on monofunctional Au-binding phage[20] and emphasize the synthesis enhancement promoted by the Au-binding peptide.

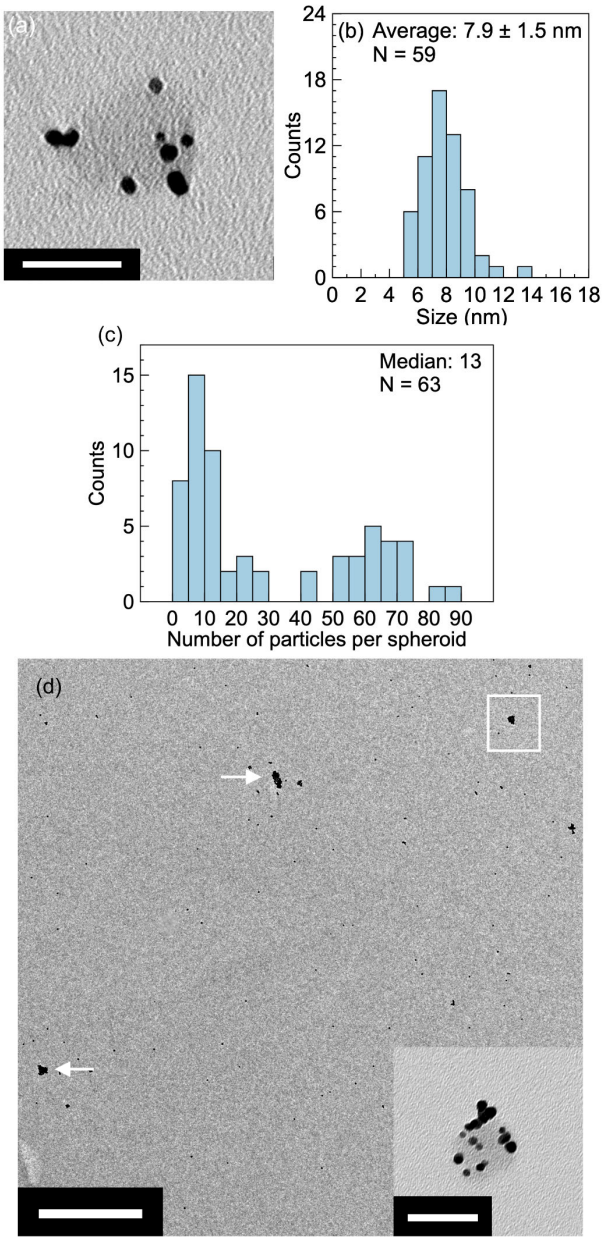

Figure 9. (a) Representative TEM image of Au/ZnS-binding spheroid after sequential ZnS and Au synthesis; scale bar: 50 nm. (b) Histogram of Au nanoparticle size distribution on Au/ZnS-binding spheroids. (c) Histogram of Au nanoparticles synthesized per spheroid. (d) Wide-field TEM of spheroids following ZnS and Au synthesis. White arrows indicate spheroids with inorganic material; scale bar: 500 nm. Inset: High magnification image of spheroid in white box; scale bar: 50 nm. Samples were not stained prior to imaging.

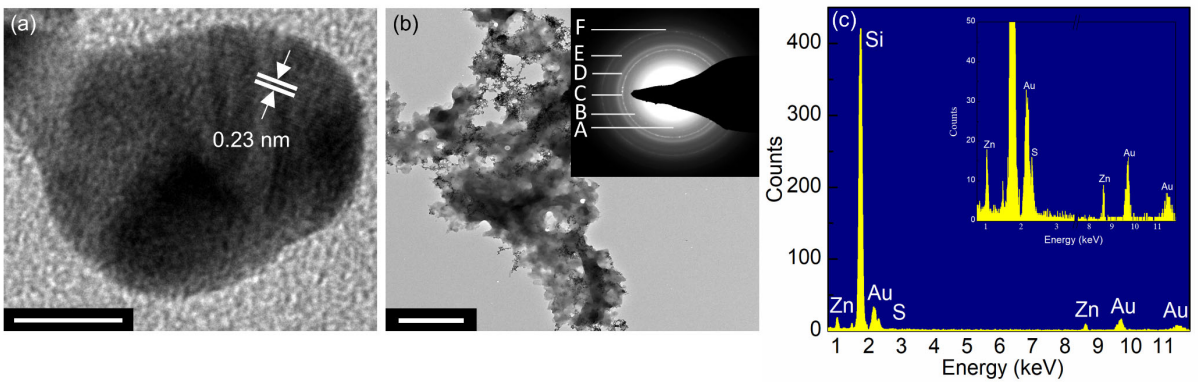

Figure 10. (a) HRTEM image of spheroid-templated Au nanoparticles synthesized after ZnS nanoparticle formation; scale bar: 5 nm. (b) Low magnification TEM image of synthesis products. Synthesis products were pelleted with high speed centrifugation prior to analysis to enhance signal; scale bar: 1 μm. Inset: Electron diffraction pattern of Au/ZnS synthesis products. Measured lattice spacings are shown in Table S1. (c) EDS spectrum of Au/ZnS-binding bifunctional nanospheroid synthesis products. Inset: EDS spectrum with scaled y-axis to emphasize elemental Zn and S peaks.

The formation of Au/ZnS nanostructures via the bifunctional template was confirmed using EDS and ED. As displayed in Figure 10 and Table S1, the elements Au, Zn, and S were present within the concentrated synthesis products and measured d-spacings were indexed to interplanar distances of both ZnS and Au. In addition, CD spectroscopy was performed following each spheroid-templated synthesis step. As shown in Figure S14, no significant difference in spheroid secondary structure was observed throughout the synthesis process. Photoluminescence spectra, also found in Figure S14, revealed reduced ZnS emission following Au synthesis. The quenching suggested non-radiative charge transfer may occur between ZnS and Au, however additional studies are needed.[44] Bifunctional M13 nanospheroids transformed with the LT process retained fusion peptide affinity on both the p3 minor coat protein and p8 major coat protein, forming robust and stable asymmetric scaffolds for synthesis of non-centrosymmetric nanostructure assemblies.

4. CONCLUSION

In summary, we have investigated the distinct progression of a M13 Au/ZnS (p8/p3)-binding bacteriophage from filament to nanospheroid and demonstrated its potential as a scaffold for non-centrosymmetric Au/ZnS nanostructure synthesis. The incorporation of the ZnS-binding motif within the p3 affected transformation, producing larger spheroids with greater loss of secondary structure than reported for Au-binding phage without a p3 peptide fusion. More work is needed to fully describe the relationship between the p3 modification and the chloroform-guided transformation process. Nonetheless, these observations have interesting implications for the versatility of the spherical template and suggest the potential to adjust nanospheroid size through p3 peptide motif design. The use of low temperature (0°C) vortex/rest cycles to produce i-forms that were subsequently converted to spheroids created more monodisperse and agglomeration resistant Au/ZnS-binding spheroids. These bifunctional spheroidal templates were used to direct sequential, site-specific synthesis of ZnS on the p3 and Au on the p8, generating non-centrosymmetric hybrid metal/semiconductor nanostructures. The ability to assemble two dissimilar and asymmetrically positioned materials on the M13 spheroid is an important achievement that significantly expands the utility and potential applications of this viral template.

†Supporting Information (SI) available: Areal densities of viral templates and agglomerates; TEM images of template morphologies and synthesis products; template size; the number and size of template ZnS and Au nanoparticles; d-spacings and crystallographic planes associated with ED patterns of synthesized ZnS and Au materials. See DOI: 10.1039/x0xx00000x

Corresponding Author

*Elaine D. Haberer, haberer@ucr.edu

Conflicts of Interest

There are no conflicts to declare

ACKNOWLEDGMENT

This material is based upon research supported by, or in part by, the U. S. Office of Naval Research under award number N00014-14-1-0799, the National Science Foundation under grant number DMR-2002941, the Regents' Faculty Fellowship, and the UCR Collaborative Seed Grant Program. This study made use of the TEM FEI Tecnai12 in the Central Facility for Advanced Microscopy and Microanalysis (CFAMM), as well as the Horiba PTI QM-400 fluorescence spectrophotometer and the Jasco J-815 CD spectrophotometer in the Analytical Chemistry Instrumentation Facility (ACIF) at UC Riverside. E.A.S.M. gratefully acknowledges fellowship support through the National Science Foundation, award number DMR-1659450. The authors acknowledge the early contributions of Esmeralda Catalan to transformation process development.

REFERENCES

(1) Petrenko, V. A.; Smith, G. P.; Gong, X.; Quinn, T. A Library of Organic Landscapes on Filamentous Phage. *Protein Eng.* **1996**, *9*, 797–801.

(2) Seker, U. O. S.; Demir, H. V. Material Binding Peptides for Nanotechnology. *Molecules* **2011**, *16*, 1426–1451.

(3) Moon, J.-S.; Kim, W.-G.; Kim, C.; Park, G.-T.; Heo, J.; Yoo, S. Y.; Oh, J.-W. M13 Bacteriophage-Based Self-Assembly Structures and Their Functional Capabilities. *Mini. Rev. Org. Chem.* **2015**, *12*, 271–281.

(4) Schick, I.; Lorenz, S.; Gehrig, D.; Tenzer, S.; Storck, W.; Fischer, K.; Strand, D.; Laquai, F.; Tremel, W. Inorganic Janus Particles for Biomedical Applications. *Beilstein J. Nanotechnol.* **2014**, *5*, 2346–2362.

(5) Qiao, Y.; Du, Y.; Zhang, X.; Li, Y. Preparation at the Water–Oil Interface of Janus Composite Nanoparticles and Their Photoelectric Properties. *J. Appl. Polym. Sci.* **2017**, *134*, 1–7.

(6) Zhang, L.; Zhang, M.; Zhou, L.; Han, Q.; Chen, X.; Li, S.; Li, L.; Su, Z.; Wang, C. Dual Drug Delivery and Sequential Release by Amphiphilic Janus Nanoparticles for Liver Cancer Theranostics. *Biomaterials* **2018**, *181*, 113–125.

(7) Li, X.; Zhou, L.; Wei, Y.; El-Toni, A. M.; Zhang, F.; Zhao, D. Anisotropic Growth-Induced Synthesis of Dual-Compartment Janus Mesoporous Silica Nanoparticles for Bimodal Triggered Drugs Delivery. *J. Am. Chem. Soc.* **2014**, *136*, 15086–15092.

(8) Schattling, P.; Thingholm, B.; Städler, B. Enhanced Diffusion of Glucose-Fueled Janus Particles. *Chem. Mater.* **2015**, *27*, 7412–7418.

(9) Jia, H.; Du, A.; Zhang, H.; Yang, J.; Jiang, R.; Wang, J.; Zhang, C. Y. Site-Selective Growth of Crystalline Ceria with Oxygen Vacancies on Gold Nanocrystals for Near-Infrared Nitrogen Photofixation. *J. Am. Chem. Soc.* **2019**, *141*, 5083–5086.

(10) Yanez-Sedeno, P.; Campuzano, S.; Pingarron, J. M. Janus Particles for (Bio)Sensing. *Appl. Mater. Today* **2017**, *9*, 276–288.

(11) Su, H.; Hurd Price, C. A.; Jing, L.; Tian, Q.; Liu, J.; Qian, K. Janus Particles: Design, Preparation, and Biomedical Applications. *Mater. Today Bio* **2019**, *4*, 1–19.

(12) Walsh, T. R.; Knecht, M. R. Biointerface Structural Effects on the Properties and Applications of Bioinspired Peptide-Based Nanomaterials. *Chem. Rev.* **2017**, *117*, 12641–

12704.

(13) Bazan, J.; Całkosiński, I.; Gamian, A. Phage Display—A Powerful Technique for Immunotherapy. *Hum. Vaccin. Immunother.* **2012**, *8*, 1829–1835.

(14) Morag, O.; Sgourakis, N. G.; Baker, D.; Goldbourt, A. The NMR–Rosetta Capsid Model of M13 Bacteriophage Reveals a Quadrupled Hydrophobic Packing Epitope. *Proc. Natl. Acad. Sci.* **2015**, *112*, 971–976.

(15) Griffith, J.; Manning, M.; Dunn, K. Filamentous Bacteriophage Contract into Hollow Spherical Particles upon Exposure to a Chloroform-Water Interface. *Cell* **1981**, *23*, 747–753.

(16) Klem, M. T.; Willits, D.; Young, M.; Douglas, T. 2-D Array Formation of Genetically Engineered Viral Cages on Au Surfaces and Imaging by Atomic Force Microscopy. *J. Am. Chem. Soc.* **2003**, *125*, 10806–10807.

(17) Royston, E.; Ghosh, A.; Kofinas, P.; Harris, M. T.; Culver, J. N. Self-Assembly of Virus-Structured High Surface Area Nanomaterials and Their Application as Battery Electrodes. *Langmuir* **2008**, *24*, 906–912.

(18) Li, F.; Chen, Y.; Chen, H.; He, W.; Zhang, Z. P.; Zhang, X. E.; Wang, Q. Monofunctionalization of Protein Nanocages. *J. Am. Chem. Soc.* **2011**, *133*, 20040–20043.

(19) Garmann, R. F.; Sportsman, R.; Beren, C.; Manoharan, V. N.; Knobler, C. M.; Gelbart, W. M. A Simple RNA-DNA Scaffold Templates the Assembly of Monofunctional Virus-Like Particles. *J. Am. Chem. Soc.* **2015**, *137*, 7584–7587.

(20) Ngo-Duc, T.-T.; Plank, J. M.; Chen, G.; Harrison, R. E. S.; Morikis, D.; Liu, H.; Haberer, E. D. M13 Bacteriophage Spheroids as Scaffolds for Directed Synthesis of Spiky Gold Nanostructures. *Nanoscale* **2018**, *10*, 13055–13063.

(21) Ngo-Duc, T. T.; Alibay, Z.; Plank, J. M.; Cheeney, J. E.; Haberer, E. D. Gold-Decorated M13 I-Forms and S-Forms for Targeted Photothermal Lysis of Bacteria. *ACS Appl. Mater. Interfaces* **2020**, *12*, 126–134.

(22) Hu, J.; Zhou, S.; Sun, Y.; Fang, X.; Wu, L. Fabrication, Properties and Applications of Janus Particles. *Chem. Soc. Rev.* **2012**, *41*, 4356–4378.

(23) Weng, L.; Zhang, H.; Govorov, A. O.; Ouyang, M. Hierarchical Synthesis of Non-Centrosymmetric Hybrid Nanostructures and Enabled Plasmon-Driven Photocatalysis. *Nat. Commun.* **2014**, *5*, 1–10.

(24) Huang, Y.; Chiang, C.; Lee, S. K.; Gao, Y.; Hu, E. L. Programmable Assembly of Nanoarchitectures Using Genetically Engineered Viruses. *Nano Lett.* **2005**, *5*, 1429–1434.

(25) Lee, S.; Mao, C.; Flynn, C. E.; Belcher, A. M. Ordering of Quantum Dots Using Genetically Engineered Viruses. *Science* **2002**, *296*, 892–895.

(26) Flynn, C. E.; Mao, C.; Hayhurst, A.; Williams, J. L.; Georgiou, G.; Iverson, B.; Belcher, A. M. Synthesis and Organization of Nanoscale II–VI Semiconductor Materials Using Evolved Peptide Specificity and Viral Capsid Assembly. *J. Mater. Chem.* **2003**, *13*, 2414–2421.

(27) Manning, M.; Chrysogelos, S.; Griffith, J. Mechanism of Coliphage M13 Contraction: Intermediate Structures Trapped at Low Temperatures. *J. Virol.* **1981**, *40*, 912–919.

(28) Manning, M.; Griffith, J. Association of M13 I-Forms and Spheroids with Lipid Vesicles. *Arch. Biochem. Biophys.* **1985**, *236*, 297–303.

(29) Berman, H. M.; Westbrook, J.; Feng, Z.; Gilliland, G.; Bhat, T. N.; Weissig, H.; Shindyalov, I. N.; Bourne, P. E. The Protein Data Bank. *Nucleic Acids Res.* **2000**, *28*, 235–242.

(30) Marvin, D. A.; Welsh, L. C.; Symmons, M. F.; Scott, W. R. P.; Straus, S. K. Molecular Structure of Fd (F1, M13) Filamentous Bacteriophage Refined with Respect to X-Ray Fibre

Diffraction and Solid-State NMR Data Supports Specific Models of Phage Assembly at the Bacterial Membrane. *J. Mol. Biol.* **2006**, *355*, 294–309.

(31) Pettersen, E. F.; Goddard, T. D.; Huang, C. C.; Couch, G. S.; Greenblatt, D. M.; Meng, E. C.; Ferrin, T. E. UCSF Chimera - A Visualization System for Exploratory Research and Analysis. *J. Comput. Chem.* **2004**, *25*, 1605–1612.

(32) Marassi, F. M.; Opella, S. J. Simultaneous Assignment and Structure Determination of a Membrane Protein from NMR Orientational Restraints. *Protein Sci.* **2003**, *12*, 403–411.

(33) Arnold, G. E.; Day, L. a; Dunker, a K. Tryptophan Contributions to the Unusual Circular Dichroism of Fd Bacteriophage. *Biochemistry* **1992**, *31*, 7948–7956.

(34) Roberts, L. M.; Dunker, A. K. Structural Changes Accompanying Chloroform-Induced Contraction of the Filamentous Phage Fd. *Biochemistry* **1993**, *32*, 10479–10488.

(35) Hoffmann-Thoms, S.; Jakob, R. P.; Schmid, F. X. Energetic Communication between Functional Sites of the Gene-3-Protein during Infection by Phage Fd. *J. Mol. Biol.* **2014**, *426*, 1711–1722.

(36) Rakonjac, J.; Model, P. Roles of PIII in Filamentous Phage Assembly. *J. Mol. Biol.* **1998**, *282*, 25–41.

(37) Nelson, F. K.; Friedman, S. M.; Smith, G. P. Filamentous Phage DNA Cloning Vectors: A Noninfective Mutant Nonh a Nonpolar Deletion in Gene III. *Virology* **1981**, *108*, 338–350.

(38) Lopez, J.; Webster, R. E. Morphogenesis of Filamentous Bacteriophage F1: Orientation of Extrusion and Production of Polyphage. *Virology* **1983**, *127*, 177–193.

(39) Rossomando, E. F.; Milstien, J. B. Electro-Optic Evidence for the Control of the Structure of Bacteriophage F1 by a Minor Coat Protein. *J. Mol. Biol.* **1971**, *58*, 187–195.

(40) Lopez, J.; Webster, R. E. Minor Coat Protein Composition and Location of the A Protein in

Bacteriophage F1 Spheroids and I-Forms. *J Virol* **1982**, *42*, 1099–1107.

(41) Marvin, D. A. Dynamics of Telescoping Inovirus: A Mechanism for Assembly at Membrane Adhesions. *Int. J. Biol. Macromol.* **1989**, *11*, 159–164.

(42) Zaman, M. S.; Moon, C. H.; Bozhilov, K. N.; Haberer, E. D. Phage-Directed Synthesis of Copper Sulfide: Structural and Optical Characterization. *Nanotechnology* **2013**, *24*, 1–8.

(43) Shen, L.; Bao, N.; Prevelige, P. E.; Gupta, A. Fabrication of Ordered Nanostructures of Sulfide Nanocrystal Assemblies over Self-Assembled Genetically Engineered P22 Coat Protein. *J. Am. Chem. Soc.* **2010**, *132*, 17354–17357.

(44) Chen, W. T.; Hsu, Y. J. L -Cysteine-Assisted Growth of Core-Satellite ZnS-Au Nanoassemblies with High Photocatalytic Efficiency. *Langmuir* **2010**, *26*, 5918–5925.

For Table of Contents Only